Nanoscale
Advances

ROYAL SOCIETY
OF CHEMISTRY

PAPER

Cite this: *Nanoscale Adv.*, 2021, **3**, 5703

Pseudocapacitive trimetallic NiCoMn-111 perovskite fluorides for advanced Li-ion supercabatteries†

Tong Yan,‡ Yongfa Huang,‡ Rui Ding,* Wei Shi, Danfeng Ying, Ziyang Jia, Caini Tan, Yuxi Huang, Xiujuan Sun and Enhui Liu

Received 4th May 2021
Accepted 9th August 2021

DOI: 10.1039/d1na00329a

rsc.li/nanoscale-advances

Exploring advanced electrochemical energy storage systems and clarifying their charge storage mechanisms are key scientific frontiers presenting a great challenge. Herein, we demonstrate a novel concept of Li-ion supercabatteries (*i.e.*, Li-ion capacitors/batteries, LICBs), which were realized using a novel trimetallic Ni–Co–Mn perovskite fluoride ($K_{0.97}Ni_{0.31}Co_{0.34}Mn_{0.35}F_{2.98}$, denoted as KNCMF-111 ($8^{\#}$)) anode and a high-performance activated carbon/$LiFePO_4$ (AC/LFP) cathode, which makes the boundary between LICs and LIBs less distinctive. Thanks to the pseudocapacitive conversion mechanism of the KNCMF-111 ($8^{\#}$) anode with superior kinetics and the enhanced capacity of the capacitor/battery hybrid AC/LFP cathode, the designed KNCMF-111 ($8^{\#}$)//AC/LFP LICBs, integrating the synergistic superiority of pseudocapacitive, capacitive and faradaic characteristics, exhibit remarkable energy/power densities and a long cycle life, indicating a high-efficiency energy storage application. Overall, this work provides new insights into exploring advanced Li-ion supercabatteries and clarifying their charge storage mechanisms based on trimetallic Ni–Co–Mn perovskite fluoride electrode materials, which sheds light on the development of advanced electrochemical energy storage systems and in-depth understanding of their charge storage mechanisms.

Introduction

Nowadays, there is an extraordinary gap between the rapidly increasing power demand for electronic information products and electric vehicles (EVs)/hybrid electric vehicles (HEVs) and the supply of renewable and high-efficiency energy, so exploring advanced electrochemical energy storage systems with high performance and renewability has always been the focus of attention and a hot topic in current scientific research.[1–4] Supercapacitors (SCs), also known as electrochemical capacitors (ECs), have been considered as one of the most promising renewable and high-efficiency electrochemical energy storage devices because of their intriguing advantages of fast kinetics, high rate capability, ultralong lifespan, *etc.*5–8 In the family of SCs, Li-ion capacitors (LICs) have received considerable attention in the last few decades and been proved to be an advanced electrochemical energy storage device, which integrates the merits of the high energy density of lithium-ion batteries (LIBs) and the high power density of SCs.[9–11] However, a serious imbalance in the aspects of kinetics and capacity exists in the anode and cathode of conventional LICs, *i.e.*, the conventional battery-type anode (*e.g.*, graphite, hard/soft carbon, *etc.*) exhibits high specific capacity but slow kinetics, while the conventional capacitive cathode (*e.g.*, activated carbon (AC)) shows fast kinetics but inferior capacity, resulting in the very unsatisfactory performance of LICs. Therefore, it is a great challenge to develop novel advanced electrochemical energy storage devices. Li-ion supercabatteries (*i.e.*, Li-ion capacitors/batteries, LICBs), as a novel concept of electrochemical energy storage devices, are believed to ensure the overall superior performance of high energy/power densities and a long cycling life.

For LICBs, however, exploring advanced electrode materials and clarifying the charge storage mechanisms (especially in the anode materials) are still a great challenge. For the anode, it is believed that exploring pseudocapacitive type candidates with rich electroactive species would contribute to both fast kinetics and high specific capacity. Recently, perovskite fluorides (ABF_3, A = K, Na, NH_4^+, *etc.*; B = Ni, Co, Mn, *etc.*) have drawn particular attention as promising anodes (such as $KNi_{0.1}Co_{0.9}F_3$, $KCo_{0.54}Mn_{0.46}F_3$/rGO, $Na_{0.85}Ni_{0.45}Co_{0.55}F_{3.57}$ and $K_{1.1}Zn_{0.83}Mn_{0.17}F_{3.03}$) for Li-based electrochemical energy storage devices from our groups, largely owing to their superior capacity, kinetics and stability.[12–15] In these studies, the redox species play a critical role in boosting the electrochemical performance of transition metal fluoride electrode materials, and multi-metal candidates

---

Key Laboratory of Environmentally Friendly Chemistry and Applications of Ministry of Education, College of Chemistry, Xiangtan University, Xiangtan, Hunan 411105, P. R. China. E-mail: drm8122@163.com; drm8122@xtu.edu.cn

† Electronic supplementary information (ESI) available. See DOI: 10.1039/d1na00329a

‡ The authors contributed equally to the work.

commonly exhibit superior behavior to their corresponding monometallic ones, largely owing to the synergistic effect of multi-metal redox species.[12–15] For Ni, Co and Mn redox species, Ni species can enhance electrochemical activity, Co species can improve the electronic conductivity and electrochemical stability, and Mn species can maintain a stable metal structure to ensure high cycle stability.[12–15] Therefore, the combination of multi-metal active species would contribute to remarkable performance. Trimetallic Ni–Co–Mn ABF_3 materials with much more complicated multi-heterostructures have been rarely reported as anodes for LICBs, and the unique interaction of multi-redox species and the charge storage mechanisms of trimetallic ABF_3 materials for Li-ion storage are still unclear. Based on the above consideration, it is a very significant challenge to explore pseudocapacitive trimetallic Ni–Co–Mn ABF_3 anode materials and clarify their charge storage mechanisms for advanced LICBs. For the cathodes, it is believed that exploring capacitor/battery type hybrid cathodes would contribute to superior kinetics and specific capacity. Activated Carbon (AC) is the first choice for the capacitive electrode material in LICs due to its advantages of low manufacturing cost, excellent resistance to chemical corrosion, a wide operating temperature range, thermal stability, abundant sources, nontoxicity, feasible processing, and easy control of the surface functional groups and the microstructure.[10,16] $LiFePO_4$ (LFP) has been selected as one of the primary battery materials for electric vehicle (EV) applications due to its flat voltage profile, low material cost, abundant material supply and better environmental compatibility compared to other cathode materials.[17,18] However, the drawbacks of pure AC (lower capacity) or LFP (inferior kinetics) are obvious, and it is expected that the construction of an AC/LFP hybrid cathode would ensure an overall superior performance when used as a cathode for LICBs.

In this work, we demonstrate novel trimetallic Ni–Co–Mn ABF_3 materials ($K_{0.97}Ni_{0.31}Co_{0.34}Mn_{0.35}F_{2.97}$, denoted as KNCMF-111 ($8^{\#}$)) as high-performance anode materials for advanced LICBs. The KNCMF-111 ($8^{\#}$) candidate exhibits a pseudocapacitive dominant conversion mechanism with superior kinetics and capacity. Moreover, the designed LICBs by matching the prelithiated KNCMF-111 ($8^{\#}$) anode and AC/LFP hybrid cathode exhibit remarkable performance, benefitting from the synergistic effect of pseudocapacitive, capacitive and faradaic responses of KNCMF-111 ($8^{\#}$), AC and LFP species during the electrochemical processes. Overall, this work addresses a new concept of LICBs based on novel trimetallic NiCoMn-111 perovskite fluorides with pseudocapacitive conversion mechanisms, which will have a significant impact on the development of advanced electrochemical energy storage systems and in-depth understanding of their charge storage mechanisms.

Results and discussion

Physicochemical properties of KNCMF-111 materials

The KNCMF-111 materials were synthesized *via* a facile one-pot solvothermal route considering the conditions of *n* (total Ni–Co–Mn metal salts)/*n* (KF) ratios, solvents, reaction temperature and time. Since the solvents are very crucial to the solvothermal synthesis, the solvent conditions were firstly studied. The X-ray diffraction (XRD) results in Fig. 1 guide us to draw the following conclusion: for the three types of solvents of ethylene glycol (EG), *n*-butanol (NBA) and *n*-propanol (NPA), it is clearly shown that an EG content in the solvents equal to or more than 50 vol% can guarantee the successful synthesis of a pure perovskite fluoride phase; therefore, the solvents for the synthesis were selected as EG, EG + NBA (1 : 1) and EG + NPA (1 : 1). Fig. 2 and S1† present the XRD patterns of KNCMF-111 ($1^{\#}$–$9^{\#}$) samples (the specific conditions are listed in Table S2†), and it can be seen that a largely pure perovskite fluoride phase can be detected and the characteristic diffraction peaks can match with the integration of standard patterns for cubic $KNiF_3$ (PDF# 21-1002), $KCoF_3$ (PDF# 18-1006) and $KMnF_3$ (PDF# 17-0116) with a $Pb\bar{3}m$ space group (the crystalline structures of KMF_3 can be seen in Fig. S2†), suggesting the successful generation of Ni–

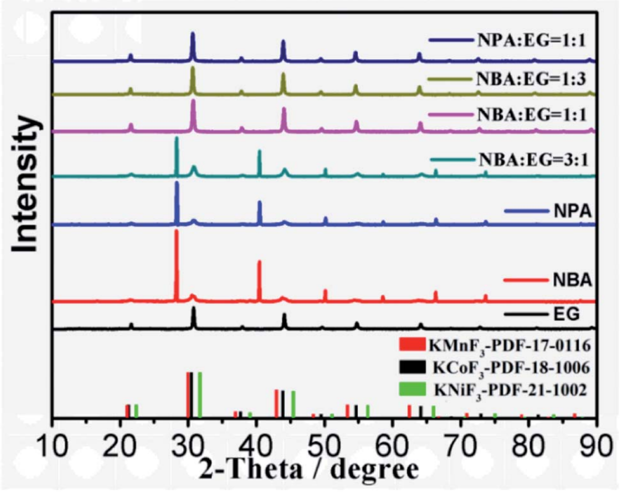

Fig. 1 The XRD patterns of as-prepared KNCMF-111 under different solvents.

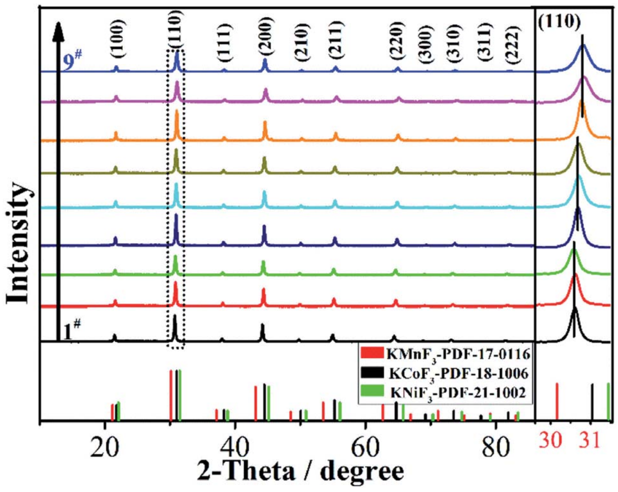

Fig. 2 XRD patterns of the KNCMF-111 ($1^{\#}$–$9^{\#}$) samples.

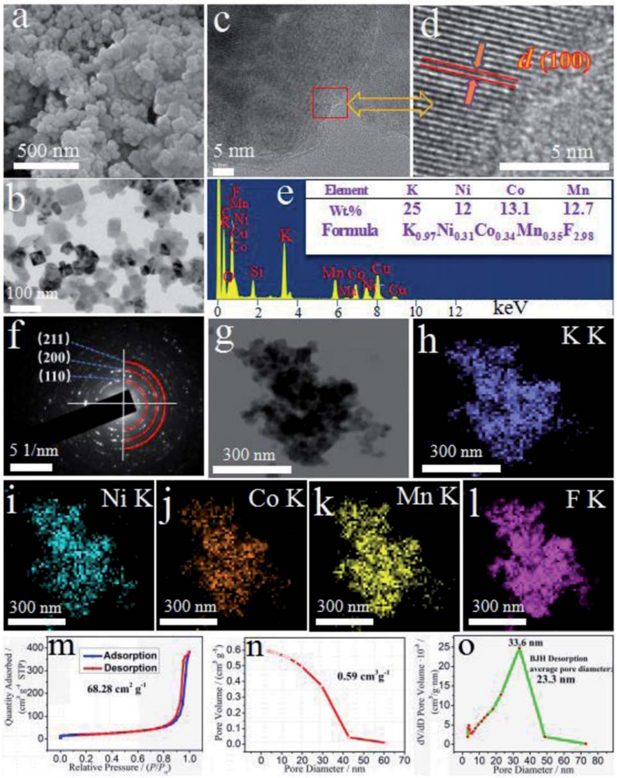

Fig. 3 SEM (a), TEM (b), HRTEM (c and d), EDS (inset shows results from ICP-MS) (e), SAED (f), mapping (g–l), N_2 isothermal sorption (m), pore volumes (n), and pore size distributions (o) of the KNCMF-111 ($8^\#$) candidate.

Co–Mn triple perovskite fluorides. Note that in the enlarged (110) crystal planes, there are slight shifts of peak positions, which can be divided into three groups ($1^\#$–$3^\#$, $4^\#$–$6^\#$ and $7^\#$–$9^\#$) in the light of the molar ratio of *n* (total Ni–Co–Mn metal salts)/*n* (KF), which may be due to the different coordination abilities and surroundings of Ni^{2+}, Co^{2+} and Mn^{2+} to F^- that influence the nucleation and growth of KNCMF-111.[14,19,20] And in each group, the peak width presents the order of $3^\# > 2^\# > 1^\#$, $6^\# > 5^\# > 4^\#$ and $9^\# \approx 8^\# > 7^\#$ largely obeying the order of ethylene glycol (EG) > EG + *n*-butanol (NBA) > EG + *n*-propanol (NPA) owing to their decreased boiling points (BPs),[14,20] reflecting the large influence of element ratios, solvents and temperatures on the structures of KNCMF-111 materials. Herein, the changes in the peak position and peak width would affect the physicochemical properties (Ni–Co–Mn heterostructure, particle size, crystallinity, *etc.*) of the trimetallic NiCoMn-111 perovskite fluorides, which will have a remarkable influence on the electrochemical performance of KNCMF-111 ($1^\#$–$9^\#$) samples discussed later.

For the optimal KNCMF-111 ($8^\#$) candidate (see the later electrochemical results), the surface morphology, particle size, element composition and distribution, specific surface area, pore volume, pore size, *etc.*, were further investigated. Fig. 3a and b depict the scanning electron microscopy (SEM) and transmission electron microscopy (TEM) images (also see Fig. S3†) of the sample, showing a rectangular/cubic nanocrystal morphology with a size range of 30–100 nm. The high resolution TEM (HRTEM) images (Fig. 3c and d) illustrate the typical (100) crystal plane, with a *d*-spacing value of about 0.41 nm, which lightly approach to the standard values of $KNiF_3$ (0.402 nm), $KCoF_3$ (0.407 nm) and $KMnF_3$ (0.419 nm) owing to the formation of NiCoMn-111 triple perovskite fluorides. The selected area electron diffraction (SAED) patterns (Fig. 3f) verify the polycrystalline characteristics for the sample with typical crystal planes of (100), (110), (200), (211), *etc.*, which is consistent with the XRD results. The X-ray energy dispersive spectra (EDS) (Fig. 3e) show the existence of K, Ni, Co, Mn and F elements, and the K/Ni/Co/Mn/F element ratio of the KNCMF-111 ($8^\#$) candidate is determined to be 0.97/0.31/0.34/0.35/2.98 by inductively coupled plasma mass spectrometry (ICP-MS) (inset of Fig. 3e) (note: the fluoride content is calculated based on the mass percentage of the whole KNCMF-111 ($8^\#$) sample (100%) minus the mass percentage of other substances (K, Ni, Co, and Mn)), which is very close to the original feeding ratio value of 1.00/0.33/0.33/0.33/3.00, further indicating the successful synthesis of the targeted NiCoMn-111 triple perovskite fluorides. Fig. 3g–l display the mapping images of the KNCMF-111 ($8^\#$) sample, which indicate a basically uniform distribution of K, Ni, Co, Mn and F elements in the sample. Fig. 3m–o depict the nitrogen sorption isotherms, pore volume and pore size distribution of the KNCMF-111 ($8^\#$) sample. The specific surface area, pore volume and average pore diameter are 68.28 $m^2\ g^{-1}$, 0.59 $cm^3\ g^{-1}$ and 23.3 nm respectively, and the pore size is mainly located at 33.6 nm, indicating a dominant mesoporous nature.[21–23]

Electrochemical behavior of KNCMF-111 electrodes

To evaluate the electrochemical properties of a series of KNCMF-111 samples for Li-ion storage, the Li//KNCMF-111 ($1^\#$–$9^\#$) half-cells were firstly investigated. The third cycle of cyclic voltammetry (CV) plots at 0.3 mV s^{-1} and galvanostatic charge–discharge (GCD) curves at 0.1 A g^{-1} in 0.01–3.0 V are shown in Fig. 4a and b respectively (CV plots for the first three cycles at 0.3 mV s^{-1} and GCD curves for the first five cycles at 0.1 A g^{-1} can be seen in Fig. S4 and S5†). In Fig. S5,† the initial coulombic efficiency of the KNCMF-111 ($1^\#$–$9^\#$) sample is less than 30%, which is mainly due to the irreversible conversion reaction and formation of a SEI film.[24,25] Note that KNCMF-111 ($8^\#$) has the largest CV area and the highest specific capacity compared to the other candidates, indicating its superior performance for Li-ion storage. Fig. 4c and d show specific capacity at 0.1–3.2 A g^{-1} and cycling behavior for 1000 cycles at 1 A g^{-1} of the KNCMF-111 ($1^\#$–$9^\#$) electrodes (more detailed performance of the $1^\#$–$9^\#$ electrodes can be seen in Fig. S6–S8† and Table S3†); the highest capacity of KNCMF-111 ($8^\#$) reaches 343 mA h g^{-1} at 0.1 A g^{-1} and remains at 63 mA h g^{-1} even at 3.2 A g^{-1}, and the KNCMF-111 ($8^\#$) electrode also exhibits favorable stability with 80% capacity retention after 400 cycles based on the value of the 10th cycle, but the stability after 1000 cycles is obviously lower than that of the KNCMF-111 ($1^\#$, $2^\#$, $4^\#$, $7^\#$) electrodes, which show however a much smaller specific capacity at 0.1–3.2 A g^{-1}. Anyway, the KNCMF-111 ($8^\#$) electrode still shows an overall superior performance to all other candidates. Note that the

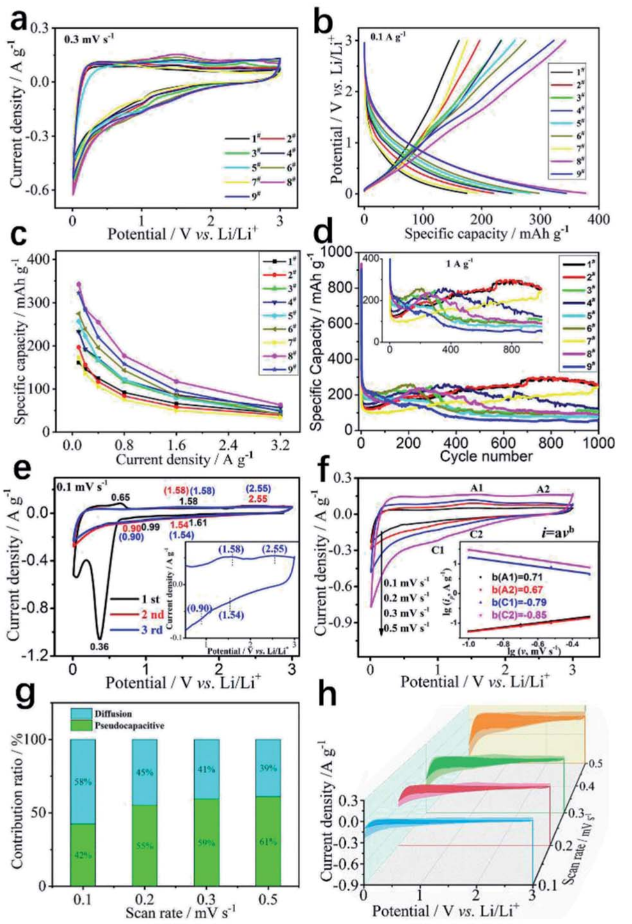

Fig. 4 CV plots at 0.3 mV s^{-1} (a), GCD curves at 0.1 A g^{-1} (b), specific capacity values at 0.1–3.2 A g^{-1} (c), and cycling stability (d) of the KNCMF-111 (1$^{\#}$–9$^{\#}$) electrodes, CV plots for the first three cycles at 0.1 mV s^{-1} and CV plots (inset) at 0.1–0.5 mV s^{-1}(e), lg *i* *vs.* lg *v* (f), pseudocapacitive ratios and corresponding CV shadow areas (g and h) of the KNCMF-111 (8$^{\#}$) electrode.

capacity of all samples fluctuated during cycling, which might be due to the following reasons:[13,26] for one thing, the activation process by the formation of a conductive metal network and an intensive pulverization process *via* the conversion mechanism (the issue will be discussed later) would facilitate local electron transport for reactions and thus increase the specific capacity; moreover, the autocatalytic process of the metal phases towards the reversible formation/decomposition of solid electrolyte interface (SEI) films is closely related to long-term activation, further enhancing the electrochemical performance; for another, the reduction of active sites by the growth of SEI films and agglomeration of amorphous particles would hinder the reactions and thus decrease the specific capacity. The specific electrochemical processes (including reaction mechanisms and kinetics) for Li-ion storage of the optimal KNCMF-111 (8$^{\#}$) electrode were further examined. Fig. 4e shows the CV plots at 0.1 mV s^{-1}, and the cathodic peaks at around 1.61 V, 0.99 V and 0.36 V in the first cycle could be assigned to be the irreversible conversion reactions between the KNCMF-111 (8$^{\#}$) electrode and Li^{+} with the products of Ni, Co, Mn, KF and LiF, and the formation of SEI films, and the anodic peaks at around 0.65 V, 1.58 V and 2.55 V during the first charging process can be attributed to the partial decomposition of SEI films and the partially reversible conversions of Ni, Co and Mn metals to NiF$_2$, CoF$_2$ and MnF$_2$.[12–15,27,28] The CV curves in the second and third cycles almost overlap, with largely repeated cathodic/anodic peaks at about 1.54, 0.9 V/1.58, and 2.55 V, verifying the good reversibility for the discharge/charge process. In addition, the first discharge specific capacity (1170 mA h g^{-1}) of the KNCMF-111 (8$^{\#}$) electrode (Fig. S5h†) is far beyond its theoretical specific capacity (352.65 mA h g^{-1}), and the extra-large specific capacity for the first discharging period would largely originate from the Li-ion intercalation reaction within the metal (Ni, Co, Mn)/LiF matrix[29–33] and the spin polarization surface capacitance at the metal (Ni, Co, Mn)/LiF interface[34,35] besides the conventional point of the formation of SEI films. Fig. 4f shows the illustration of CV plots at 0.1, 0.2, 0.3 and 0.5 mV s^{-1} of the KNCMF-111 (8$^{\#}$) electrode, and as depicted, two pairs of redox peaks (A1/C1 and A2/C2) discussed above are present in the CV plots, which are ascribed to be the largely reversible conversion reactions; note that the slopes of the lg $i \sim$ lg ν plots (inset of Fig. 4f) for anodic and cathodic processes are 0.67, 0.71/−0.79, and −0.85, indicating that the kinetic behavior is a surface/diffusion mixed control property,[13–15,36] and the pseudocapacitive ratios (Fig. 4g and h) at 0.1, 0.2, 0.3 and 0.5 mV s^{-1} were calculated to be 42, 55, 59 and 61% respectively based on the equation $i = k_1\nu + k_2\nu^{0.5}$, showing the dominating pseudocapacitive behavior. It is reported that, when designing diffusion-controlled battery materials on the nanoscale, there will also be 'extrinsic' pseudocapacitance, so that most of the Li^{+} storage sites are located on the surface or near the surface area.[37] Furthermore, the solid-state diffusion of Li^{+} was investigated through the GITT (galvanostatic intermittent titration technique). As can be seen in Fig. S9,† the D_{Li} ranged from 10^{-9} to 10^{-8} cm^{2} s^{-1} during the lithiation and delithiation processes, which enables the fast solid-state diffusion of Li^{+} in KNCMF-111 (8$^{\#}$). All in all, benefitting from the unique properties of extrinsic pseudocapacitive behavior and a high diffusion coefficient, KNCMF-111 (8$^{\#}$) might display good charge–discharge performance.

Ex situ X-ray photoelectron spectroscopy (XPS) and TEM-SAED-EDS mapping tests were performed to reveal the conversion mechanism of the KNCMF-111 (8$^{\#}$) electrode for Li-ion storage. As shown in Fig. 5, the surface species, chemical bonds and electronic structures of the pristine and fully discharged and charged states (after the first cycle of discharging/charging processes at 0.1 A g^{-1}, Fig. S10†) for the 8$^{\#}$ electrode were checked. In the survey scans of the three states (Fig. 5a), the targeted signals of K2p, Ni2p, Co2p, Mn2p, F1s, C1s, O1s and Li1s (only for the discharged/charged states) can be detected respectively. And the Ni2p, Co2p, and Mn2p spectra (Fig. 5b–d) present the typical M2p3/2/M2p1/2 (M = Ni, Co, Mn) peaks along with their shakeup satellite peaks (Sat). The peak positions of Ni2p, Co2p and Mn2p of the fully discharged/charged states show obviously negative shifts (−1.9, −1.8, and −1.2 eV) compared with those of pristine states, indicating the presence of Ni, Co, and Mn metal phases during the discharging/

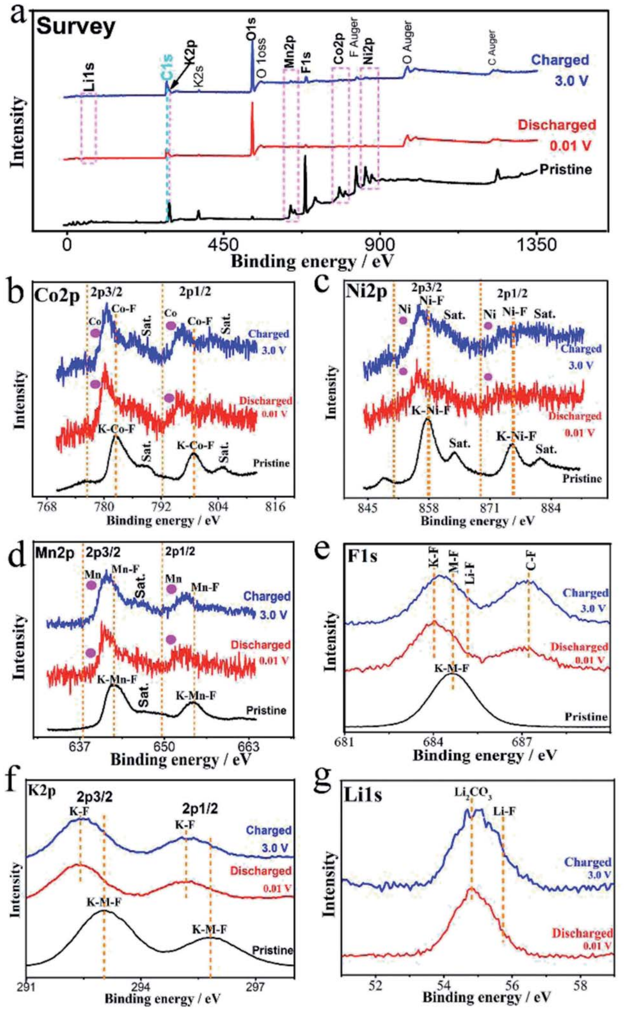

Fig. 5 *Ex situ* XPS spectra for survey (a), Co2p (b), Ni2p (c), Mn2p (d), F1s (e), K2p (f), and Li1s (g) of the KNCMF-111 ($8^{\#}$) electrode in the pristine and/or fully discharged/charged states (after the 1st/2nd segments of GCD tests at 0.1 A g^{-1}).

charging processes.[12–15] The F1s and K2p spectra in Fig. 5e and f also show negative shifts (−0.6 and −0.8 eV) for the fully discharged/charged states in comparison with the pristine states, suggesting the changes of surface chemical conditions of F and K species (no longer the complete KMF_3 structure of the pristine state); the F1s spectra reveal the K–F, M–F (M = Ni, Co, Mn), Li–F and C–F (from the PVDF binder) bonds for the fully discharged/charged states, whereas only the K–M–F structure can be resolved for the pristine state, suggesting the participation of MF_2 and LiF phases in the conversion reactions, and the K2p spectra further indicate the existence of K–F new phases for the discharging/charging process. The Li1s signals (Fig. 5g) of the fully discharged/charged states contain the Li_2CO_3 and LiF phases, and the O1s signals of the fully discharged/charged states are much stronger than those of the pristine state, which are indicative of the formation of SEI films.[12–15] Furthermore, the above indicated conversion products (Ni, Co, Mn, KF, LiF, Li_2CO_3/Ni, Co, Mn, KF, LiF, Li_2CO_3, NiF_2, CoF_2, and MnF_2)

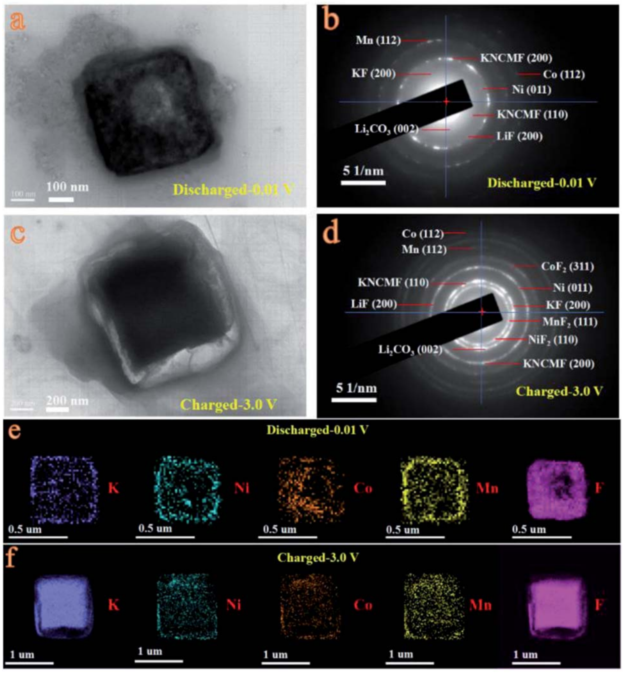

Fig. 6 *Ex situ* TEM images (a and c), SAED spectra (b and d) and EDS mapping (e and f) of the KNCMF-111 ($8^{\#}$) electrode in the first fully discharged/charged states (after the 1st/2nd segments of GCD tests at 0.1 A g^{-1}).

along with the unreacted KNCMF perovskite phase of the fully discharged/charged states can be well detected from the *ex situ* TEM-SAED-EDS mapping patterns (Fig. 6). Based on the above analysis, the KNCMF-111 ($8^{\#}$) electrode exhibits a typical surface conversion reaction mechanism for the Li-ion storage, integrated with the partial contribution of a largely reversible SEI formation/decomposition reaction, the possible Li-ion intercalation reaction within the metal (Ni, Co, Mn)/LiF matrix and spin polarization surface capacitance at the metal (Ni, Co, Mn)/LiF interface, which can be deduced as the following eqn (1)–(5):

$$x\mathrm{ABF_3} + 2x\mathrm{Li}^+ + 2x\mathrm{e}^- \rightarrow x\mathrm{B} + x\mathrm{AF} + 2x\mathrm{LiF} \qquad (1)$$

$$y\mathrm{B} + 2y\mathrm{LiF} \leftrightarrow y\mathrm{BF_2} + 2y\mathrm{Li}^+ + 2y\mathrm{e}^- \qquad (2)$$

$$\mathrm{Li}^+ + \text{electrolytes} + \mathrm{e}^- \leftrightarrow \text{SEI films} \qquad (3)$$

$$z\mathrm{Li}^+ + z\mathrm{e}^- + x\mathrm{B}/2x\mathrm{LiF} \leftrightarrow x\mathrm{B}/z\mathrm{Li}/2x\mathrm{LiF} \qquad (4)$$

$$z'\mathrm{Li}^+ + z'\mathrm{e}^- + x\mathrm{B}/2x\mathrm{LiF} \leftrightarrow z'\mathrm{Li}/x\mathrm{B}/2x\mathrm{LiF} \qquad (5)$$

where A = K; B = Ni, Co, Mn; $0 < x < 1$; $0 < y, z, z' < x$.

The LICs based on the optimal KNCMF-111 ($8^{\#}$) material were further evaluated (the $m+/m-$ ratios were designed based on the charge balance in Table S4†). Firstly, the superior KNCMF-111 candidates ($1^{\#}$, $2^{\#}$, $4^{\#}$, $7^{\#}$, and $8^{\#}$) and precharging model were examined; based on the results (Fig. S11 and S12†), one can see that the KNCMF-111 ($8^{\#}$) material is indeed a relatively superior candidate for LICs and the performance of ($8^{\#}$)//AC LICs can be largely enhanced by the precharging (here meaning prelithiation) treatment at 0.1 A g^{-1} (Fig. S13–S15†). It is said that the prelithiation not only forms more complete SEI films but also increases the content of active Li, providing a more stable structure.[15,38] The electrochemical performance of $8^{\#}$-P//AC LICs with the anode precharged at 0.1 A g^{-1} at the working voltages of 0–4.0, 4.3, 4.5 and 4.7 V were further examined, and the results are shown in Fig. 8a–d. It is demonstrated that the $8^{\#}$-P//AC LICs with working voltages of 0–4.3 V (101.60–18.64 Wh kg^{-1}/0.26–8.39 kW kg^{-1}, and 82%/4000 cycles/10 A g^{-1}) and 0–4.5 V (116.16–25.85 Wh kg^{-1}/0.27–8.78 kW kg^{-1}, and 70%/4000 cycles/10 A g^{-1}) exhibit a relatively overall superior performance to the other two LICs with working voltages of 0–4.0 V (79.54–15.18 Wh kg^{-1}/0.24–7.81 kW kg^{-1}, and 90%/4000 cycles/10 A g^{-1}) and 0–4.7 V (136.50–32.10 Wh kg^{-1}/0.29–9.17 kW kg^{-1}, and 60%/3000 cycles/10 A g^{-1}) (CV plots at 10–160 mV s^{-1}, GCD plots at 0.5–16 A g^{-1}, cycling plots and performance summary of the $8^{\#}$-P//AC LICs at 0–4.0, 4.3, 4.5 and 4.7 V with the anode precharged at 0.1 A g^{-1} are shown in Fig. S16, and Table S5†).

To further enhance the performance of the $8^{\#}$-P//AC LICs, the novel concept of LICBs was therefore designed. Firstly, the capacitive-type AC cathode was modified with a faradaic-type cathode including $LiFePO_4$ (LFP) and $LiMn_2O_4$ (LMO) with a larger specific capacity. Fig. 7 illustrates the performance of the AC, AC + LMO (1 : 1 in weight), and AC + LFP (1 : 1 in weight) electrodes. AC shows the typical physical sorption properties of the electric double layer (EDL) electrode. It's well known that LMO and LFP exhibit the typical faradaic behavior of battery electrodes, so AC + LFP (1 : 1) and AC + LMO (1 : 1) undergo the EDL and faradaic hybrid mechanisms (CV plots/GCD curves at different scan rates/current densities can be seen in Fig. S17†). Based on the results, one can see that the AC + LFP (1 : 1) capacitive-faradaic hybrid cathode shows superior performance involving larger reversible specific capacity, high rate capability and long cycling life, so AC + LFP (1 : 1) was selected as the cathode material to construct LICBs to enhance the performance of LICs.

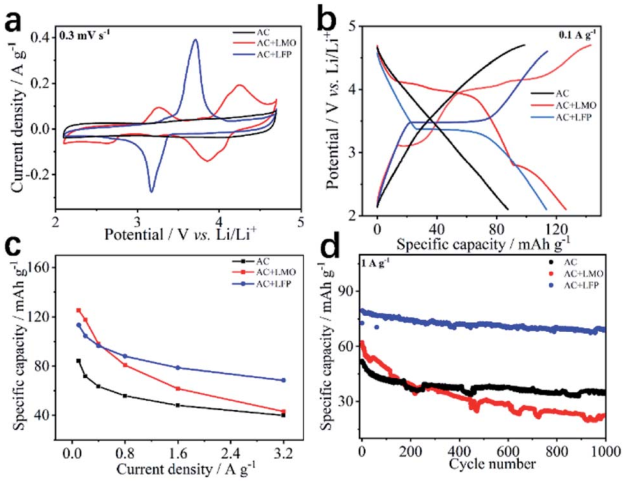

Fig. 7 The CV plots at 0.3 mV s^{-1} (a), GCD curves at 0.1 A g^{-1} (b), specific capacity at 0.1–3.2 A g^{-1} (c) and cycling behavior for 1000 cycles at 1 A g^{-1} of (d) AC, AC + LMO (1 : 1) and AC + LFP (1 : 1) electrodes.

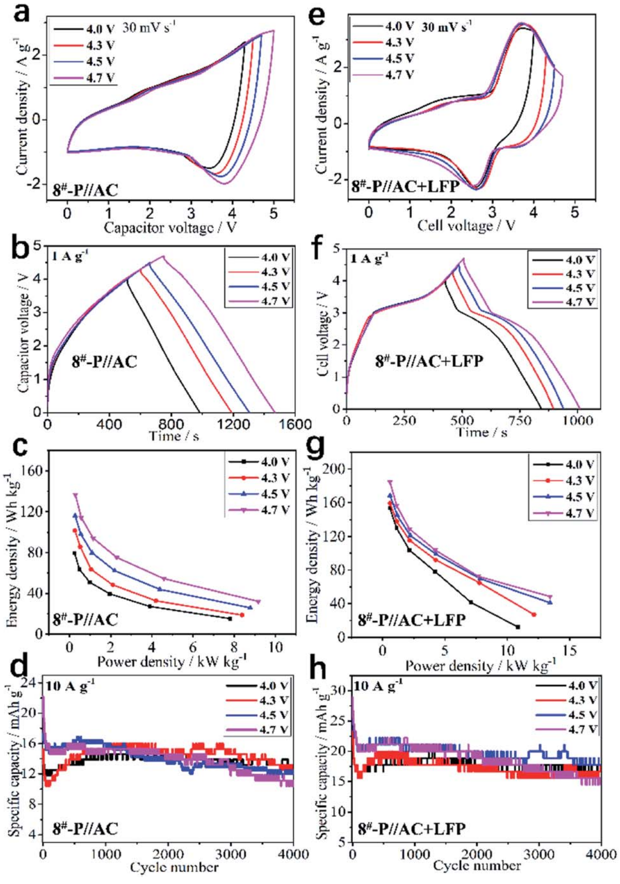

Fig. 8 CV plots at 30 mV s^{-1} (a), GCD curves at 1 A g^{-1} (b), Ragone plots (c), and cycling stability (d) of $8^{\#}$-P//AC LICs at 0–4, 0–4.3,0–4.5 and 0–4.7 V, CV plots at 10 mV s^{-1} (e), GCD curves at 1 A g^{-1}, (f) Ragone plots (g), and cycling stability (h) of $8^{\#}$-P//AC + LFP LICBs at 0–4, 0–4.3,0–4.5 and 0–4.7 V.

The electrochemical performance of the $8^{\#}$-P//AC + LFP (1 : 1) LICBs at different working voltages (0–4.0, 4.3, 4.5, and 4.7 V) was further examined, and the results are shown in Fig. 8e–h, which behave more like a battery, demonstrating a remarkable performance in a wide working voltage range of 0–4.7 V (0–4.0 V, 153.26–12.09 Wh kg^{-1}/0.58–10.88 kW kg^{-1}, and 84%/4000 cycles/10 A g^{-1}; 0–4.3 V, 159.25–27.02 Wh kg^{-1}/0.59–12.16 kW kg^{-1}, and 76%/4000 cycles/10 A g^{-1}; 0–4.5 V, 168.39–41.07 Wh kg^{-1}/0.59–13.44 kW kg^{-1}, and 70%/4000 cycles/10 A g^{-1}; 0–4.7 V, 184.77–48.53 Wh kg^{-1}/0.58–13.44 kW kg^{-1}, and 60%/3000 cycles/10 A g^{-1}), which are all superior to that of the corresponding $8^{\#}$-P//AC LICs. More importantly, the performance of $8^{\#}$-P//AC + LFP (1 : 1) LICBs is superior to that of many reported state-of-the-art LICs and also LIBs (Table S7†) (the CV plots at 10–160 mV s^{-1}, GCD plots at 0.5–16 A g^{-1}, cycling plots and performance summary of the 8#-P//AC + LFP (1 : 1) LICBs at 0–4.0, 4.3, 4.5 and 4.7 V with the anode precharged at 0.1 A g^{-1} are shown in Fig. S18 and Table S6†). Based on the above results, the LICBs with the KNCMF-111 ($8^{\#}$) perovskite fluoride electrode materials show very attractive potential for application in advanced energy storage systems.

Conclusions

In summary, we have demonstrated a new concept of advanced LICBs with novel trimetallic NiCoMn-111 perovskite fluoride electrode materials, showing typical pseudocapacitive conversion mechanisms with superior kinetics and capacity. Owing to the synergistic effect of capacitive, pseudocapacitive and faradaic behavior, the designed LICB based on the KNCMF-111 ($8^{\#}$-P) anode and AC + LFP (1 : 1) cathode exhibits remarkable energy/power densities and cycling performance. All in all, this study highlights new insights into exploring advanced Li-ion supercabatteries and clarifying their charge storage mechanisms based on KNCMF-111 perovskite fluoride electrode materials, demonstrating a high impact on developing advanced electrochemical energy storage systems.

Experimental section

Synthesis of KNCMF-111 materials

Analytical/guaranteed reagents (AR/GR) were directly used in the experiment (Table S1†). The synthesis of nine KNCMF-111 materials was carried out under specific experimental conditions (Table S2†). As an example, for the synthesis of the KNCMF-111 ($8^{\#}$) sample: firstly, 0.66 mmol $NiCl_2 \cdot 6H_2O$, 0.66 mmol $CoCl_2 \cdot 6H_2O$, 0.66 mmol $MnCl_2 \cdot 4H_2O$, 5.94 mmol $KF \cdot 2H_2O$ and 0.2 g PVP-K30 were added into 40 ml mixed solvents, which were composed of EG and NBA with a volume ratio of 1 : 1; next, the mixture was stirred thoroughly and dispersed by using an ultrasonic bath for 30 minutes before it was transferred into a 50 ml Teflon-lined stainless steel autoclave, which was then placed in an electric oven at 160 °C for 24 h and naturally cooled down to room temperature; finally, the product was collected by centrifugal filtration along with washing with absolute alcohol several times, and further dried at 95 °C overnight. Seven samples for studying the solvents were also synthesized based on the same route mentioned above except the specific solvents (EG, NBA, NPA, NBA : EG (3 : 1, 1 : 1, and 1 : 3), and NPA : EG(1 : 1)), and the fixed reaction temperature and time (180 °C/6 h).

Characterization

The characteristics of the phase properties and crystal structure were characterized by X-ray diffraction (XRD). The information of the surface morphology and particle size was obtained by scanning electron microscopy (SEM) and transmission electron microscopy (TEM). The deeper crystalline microstructures were characterized by high-resolution TEM (HRTEM) and selected area electron diffraction (SAED). The elemental composition and distribution were resolved by X-ray energy dispersive spectroscopy (EDS), inductively coupled plasma mass spectrometry (ICP-MS) and mapping. The surface chemical compositions and electronic structures were determined by X-ray photoelectron spectroscopy (XPS). The specific surface area, pore volume and pore size distribution were analyzed by nitrogen isothermal sorption analysis with Brunauer–Emmett–Teller (BET) and Barrett–Joyner–Halenda (BJH) methods.

Electrochemical measurements

Electrode preparation. Briefly, the electrodes were prepared by casting the well-mixed slurry on the current collectors (copper or carbon-coated aluminum foil for the anode/cathode respectively), followed by thorough drying at 110 °C for 12 h in a vacuum, and then punched into disks with a diameter of 12 mm. The mixed slurry was made up of specific active materials (KNCMF-111, AC, $LiFePO_4$ (LFP), and AC + LFP (1 : 1 in weight)), acetylene black (AB) conductive agent and polyvinylidene fluoride (PVDF) binder in a weight ratio of 7/2/1, which was dissolved in *N*-methyl-2-pyrrolidone (NMP). The active mass loading of the electrodes was about 1.2 mg cm^{-2}, while fabricating the half cell. And when fabricating the full cell device, the active mass loading of the electrodes was based on the mass ratio of cathode/anode (m+/m−) (Table S4†), the cathode loading was about 1.8–3.8 mg cm^{-2}, and the anode loading was about 1.2 mg cm^{-2}.

Assembly of LICs and LICBs

The LICs and LICBs were assembled with untreated KNCMF-111 ($1^{\#}$, $2^{\#}$, $4^{\#}$, $7^{\#}$, $8^{\#}$) or prelithiated KNCMF-111 ($8^{\#}$) anodes, AC or AC + LFP cathodes and a glass fiber (GF) separator by using 2032 coin cells. The electrolytes were 1 M $LiPF_6$ dissolved in the mixed solvents of ethylene carbonate (EC), ethyl methyl carbonate (EMC) and dimethyl carbonate (DMC) (1 : 1 : 1 in volume) with 1% vinylene carbonate (VC) additives (LBC-305-01, CAPCHEM).

Tests and calculations

The electrochemical tests were conducted by cyclic voltammetry (CV) with CHI660E electrochemical workstations and galvanostatic charge–discharge (GCD) with Neware-CT-4008 testers. A typical two-electrode device, with the electrode of active materials and a Li plate as the working electrode (WE) and counter/reference electrodes (CE/RE), was used for the tests of electrodes, and a typical two-electrode device (above assembled LICs and LICBs) was used for the tests of full cells. The mass ratio of cathode/anode (m+/m−), the specific capacity (C_m, mAh g^{-1}) for electrodes/LICs/LICBs, and energy density (E_m, Wh kg^{-1})/power density (P_m, kW kg^{-1}) for LICs/LICBs were calculated based on eqn (6)–(10).

$$m(+)/m(-) = C_m(-)/C_m(+) \tag{6}$$

$$C_m = Q/3.6m \tag{7}$$

$$E_m\ (\text{LICs}) = (Q_m \Delta V)/2 \tag{8}$$

$$E_m\ (\text{LICBs}) = C_m V \tag{9}$$

$$P_m = 3.6E_m/t_d \tag{10}$$

where m, Q, ΔV, V and t_d refer to the mass of active materials (g) (for single electrodes or half cells, it indicates the mass of the anode or cathode material; for LICs/LICBs, the mass means the sum of masses of anode and cathode materials), capacity (C, for the cathode/anode, it respectively indicates the discharging/charging quantity; for full cells, it means the discharging quantity), voltage window (V), discharging plateau voltage (V), and discharging time (s), respectively.

The solid diffusion coefficient was calculated based on the equation as follows:

$$D^{\mathrm{GITT}} = \frac{4}{\pi\tau}\frac{m_{\mathrm{B}}V_{\mathrm{M}}}{(M_{\mathrm{B}}S)^2}\frac{\Delta E_{\mathrm{S}}}{(\Delta E_{\mathrm{t}})^2} \tag{11}$$

where the duration of the current pulse (s) is represented by t, τ is the relaxation time (s), m_{B} is the mass of the active substance, V_{M} is the molar volume, M_{B} is the molar mass, S is the electrode/electrolyte contact area, ΔE_{s} means the steady-state potential change (V) by the current pulse, and ΔE_{t} is the potential change (V) during the constant current pulse after eliminating the iR drop.

Conflicts of interest

There are no conflicts to declare.

Acknowledgements

The financial support from the National Natural Science Foundation of China (22078279) is acknowledged.

Notes and references

1 B. Dunn, H. Kamath and J.-M. Tarascon, *Science*, 2011, **334**, 928–935.

2 S. Chu and A. Majumdar, *Nature*, 2012, **488**, 294–303.

3 K. Naoi, S. Ishimoto, J.-i. Miyamoto and W. Naoi, *Energy Environ. Sci.*, 2012, **5**, 9363–9373.

4 X. Wang, X. Lu, B. Liu, D. Chen, Y. Tong and G. Shen, *Adv. Mater.*, 2014, **26**, 4763–4782.

5 J. R. Miller and P. Simon, *Science*, 2008, **321**, 651–652.

6 P. Simon and Y. Gogotsi, *Nat. Mater.*, 2008, **7**, 845–854.

7 Y. Wang, Y. Song and Y. Xia, *Chem. Soc. Rev.*, 2016, **45**, 5925–5950.

8 F. Wang, X. Wu, X. Yuan, Z. Liu, Y. Zhang, L. Fu, Y. Zhu, Q. Zhou, Y. Wu and W. Huang, *Chem. Soc. Rev.*, 2017, **46**, 6816–6854.

9 V. Aravindan, J. Gnanaraj, Y.-S. Lee and S. Madhavi, *Chem. Rev.*, 2014, **114**, 11619–11635.

10 B. Li, J. Zheng, H. Zhang, L. Jin, D. Yang, H. Lv, C. Shen, A. Shellikeri, Y. Zheng, R. Gong, J. P. Zheng and C. Zhang, *Adv. Mater.*, 2018, **30**, 1705670.

11 P. Jeżowski, O. Crosnier, E. Deunf, P. Poizot, F. Béguin and T. Brousse, *Nat. Mater.*, 2018, **17**, 167–173.

12 Q. Xu, R. Ding, W. Shi, D. Ying, Y. Huang, T. Yan, P. Gao, X. Sun and E. Liu, *J. Mater. Chem. A*, 2019, **7**, 8315–8326.

13 D. Ying, R. Ding, Y. Huang, W. Shi, Q. Xu, C. Tan, X. Sun, P. Gao and E. Liu, *J. Mater. Chem. A*, 2019, **7**, 18257–18266.

14 W. Shi, R. Ding, Q. Xu, T. Yan, Y. Huang, C. Tan, X. Sun, P. Gao and E. Liu, *Chem. Commun.*, 2019, **55**, 6739–6742.

15 D. Ying, Q. Xu, R. Ding, Y. Huang, T. Yan, Y. Huang, C. Tan, X. Sun, P. Gao and E. Liu, *Chem. Eng. J.*, 2020, **388**, 124154.

16 H. Wang, C. Zhu, D. Chao, Q. Yan and H. J. Fan, *Adv. Mater.*, 2017, **29**, 1702093.

17 W.-J. Zhang, *J. Power Sources*, 2011, **196**, 2962–2970.

18 M. Wang, Y. Yang and Y. Zhang, *Nanoscale*, 2011, **3**, 4434–4439.

19 D. Ying, Y. Li, R. Ding, W. Shi, Q. Xu, Y. Huang, Z. Jia, W. Yu, X. Sun, P. Gao, E. Liu and X. Wang, *Adv. Funct. Mater.*, 2021, **31**, 2101353.

20 Y. Huang, R. Ding, D. Ying, Y. Huang, C. Tan, T. Yan, X. Sun and E. Liu, *Chem. Commun.*, 2021, **57**, 7705–7708.

21 R. Ding, L. Qi, M. Jia and H. Wang, *Electrochim. Acta*, 2013, **107**, 494–502.

22 R. Ding, X. Li, W. Shi, Q. Xu, X. Han, Y. Zhou, W. Hong and E. Liu, *J. Mater. Chem. A*, 2017, **5**, 17822–17827.

23 W. Shi, R. Ding, X. Li, Q. Xu, D. Ying, Y. Huang and E. Liu, *Chem.–Eur. J.*, 2017, **23**, 15305–15311.

24 C. Tan, R. Ding, Y. Huang, T. Yan, Y. Huang, F. Yang, X. Sun, P. Gao and E. Liu, *Electrochim. Acta*, 2021, **389**, 138713.

25 C. Tan, R. Ding, Y. Huang, T. Yan, Y. Huang, F. Yang, X. Sun, P. Gao and E. Liu, *Chem. Commun.*, 2021, **57**, 5830–5833.

26 Y. Huang, X. Li, R. Ding, D. Ying, T. Yan, Y. Huang, C. Tan, X. Sun, P. Gao and E. Liu, *Electrochim. Acta*, 2020, **329**, 135138.

27 K. Rui, Z. Wen, Y. Lu, J. Jin and C. Shen, *Adv. Energy Mater.*, 2015, **5**, 1401716.

28 F. Wang, R. Robert, N. A. Chernova, N. Pereira, F. Omenya, F. Badway, X. Hua, M. Ruotolo, R. Zhang, L. Wu, V. Volkov, D. Su, B. Key, M. S. Whittingham, C. P. Grey, G. G. Amatucci, Y. Zhu and J. Graetz, *J. Am. Chem. Soc.*, 2011, **133**, 18828–18836.

29 S. Grugeon, S. Laruelle, R. Herrera-Urbina, L. Dupont, P. Poizot and J. M. Tarascon, *J. Electrochem. Soc.*, 2001, **148**, A285.

30 H. Li, G. Richter and J. Maier, *Adv. Mater.*, 2003, **15**, 736–739.

31 J. Tan, L. Liu, S. Guo, H. Hu, Z. Yan, Q. Zhou, Z. Huang, H. Shu, X. Yang and X. Wang, *Electrochim. Acta*, 2015, **168**, 225–233.

32 S. Laruelle, S. Grugeon, P. Poizot, M. Dollé, L. Dupont and J. M. Tarascon, *J. Electrochem. Soc.*, 2002, **149**, A627.

33 Y.-Y. Hu, Z. Liu, K.-W. Nam, O. J. Borkiewicz, J. Cheng, X. Hua, M. T. Dunstan, X. Yu, K. M. Wiaderek, L.-S. Du, K. W. Chapman, P. J. Chupas, X.-Q. Yang and C. P. Grey, *Nat. Mater.*, 2013, **12**, 1130–1136.

34 Q. Li, H. Li, Q. Xia, Z. Hu, Y. Zhu, S. Yan, C. Ge, Q. Zhang, X. Wang, X. Shang, S. Fan, Y. Long, L. Gu, G.-X. Miao, G. Yu and J. S. Moodera, *Nat. Mater.*, 2021, **20**, 76–83.

35 T. Yan, R. Ding, Y. Huang, D. Ying, C. Tan, Y. Huang, F. Yang, X. Sun, P. Gao and E. Liu, *J. Mater. Chem. A*, 2021, **9**, 14276–14284.

36 V. Augustyn, J. Come, M. A. Lowe, J. W. Kim, P.-L. Taberna, S. H. Tolbert, H. D. Abruña, P. Simon and B. Dunn, *Nat. Mater.*, 2013, **12**, 518–522.

37 P. Simon, Y. Gogotsi and B. Dunn, *Science*, 2014, **343**, 1210–1211.

38 N. Gunawardhana, G.-J. Park, A. K. Thapa, N. Dimov, M. Sasidharan, H. Nakamura and M. Yoshio, *J. Power Sources*, 2012, **203**, 257–261.